Water Reduction

DOI: 10.1002/anie.201409813

Ligand Transformations and Efficient Proton/Water Reduction with Cobalt Catalysts Based on Pentadentate Pyridine-Rich Environments**

Debashis Basu, Shivnath Mazumder, Xuetao Shi, Habib Baydoun, Jens Niklas, Oleg Poluektov, H. Bernhard Schlegel, and Cláudio N. Verani**

Abstract: *A series of cobalt complexes with pentadentate pyridine-rich ligands is studied. An initial Co^{II} amine complex **1** is prone to aerial oxidation yielding a Co^{III} imine complex **2** that is further converted into an amide complex **4** in presence of adventitious water. Introduction of an N-methyl protecting group to the ligand inhibits this oxidation and gives rise to the Co^{II} species **5**. Both the Co^{III} **4** and Co^{II} **5** show electrocatalytic H_2 generation in weakly acidic media as well as in water. Mechanisms of catalysis seem to involve the protonation of a Co^{II}–H species generated in situ.*

The ever-increasing demand for alternative energy sources along with the continuous decline of fossil fuel reserves have driven extensive research on water splitting aiming to generate dihydrogen.[1] Earth-abundant transition metals like cobalt, nickel, and iron are of immense interest due to their ability to electrocatalyze the formation of dihydrogen from acidic solutions.[2] Cobalt is chief among these metals due to its energetically affordable conversions from $3d^6$ Co^{III} to $3d^7$ Co^{II} to nucleophilic $3d^8$ Co^{I} species, and has been extensively used.[3] Cobalt oximes figure among the most studied examples used for proton reduction.[4] The π-accepting nature of these ligands stabilizes the Co^{I} state that takes up a proton to generate cobalt/hydride species Co^{III}–H^- amenable to reduction to Co^{II}–H^-. The latter species subsequently reacts with a second proton to generate H_2.[5] Recent results point to the importance of pyridine-containing ligands in proton reduction, for which complexes of imino-, di-, tetra-, and pentapyridine ligands have been investigated.[6] Several of these systems are also water-soluble, and therefore relevant for direct water reduction.

Our groups have a long-standing interest in redox-active phenylenediamine-bridged pentadentate $[N_2O_3]$ ligands capable of forming stable first-row transition metal complexes.[7] Thus far we emphasized phenolate-rich environments, and observed a facile conversion from the secondary amine to imine. While Fe^{III} species have been used in current rectifying devices,[7e,f] Co^{III} complexes are electrocatalysts for proton reduction in trifluoroacetic acid/MeCN.[7g] However, these species have intrinsic negative overpotentials, and we hypothesized that similar $[N_2N^{py}_3]$ pentadentate pyridine-rich environments would yield affordable catalysis and water solubility. Such systems allow the proton to bind to the sixth position of the metal in a framework that is potentially redox-active and a π-acceptor, thus contributing to the stabilization of the Co^{I} state.

The $[N_2N^{py}_3]$ ligand L^{1H} was obtained by treatment of phenylenediamine with picolyl chloride in water and in the presence of sodium hydroxide and hexadecyl trimethyl ammonium chloride.[8] The purified ligand was treated with $CoCl_2{\cdot}6H_2O$ in methanol under aerobic conditions for 3 h and followed by counterion exchange with $NaClO_4$. An initial pink solution containing $[Co^{II}(L^{1H})Cl]^{2+}$ turned greenish within minutes and yielded a crystalline mixture of an orange $[Co^{III}(L^{1C=N})Cl](ClO_4)_2$ (**2**) and a green $[Co^{III}(L^{1OMe})Cl]ClO_4$ (**3**) species after two days (Scheme 1). When the mother liquor was allowed to stand for 5–7 days, light-orange crystals of $[Co^{III}(L^{1C=O})Cl]ClO_4$ (**4**) were obtained. Identical results were obtained by recrystallizing the mixture of **2** and **3** from either MeCN/diethyl ether (1:1) or ethanol/acetone (1:1). Furthermore, species **4** can be generated directly upon complexation of L^{1H} and $CoCl_2{\cdot}6H_2O$ in acetone/water (1:1) at room temperature after 5–7 days under aerobic conditions.

Complexes **2**–**4** have been characterized spectroscopically by FTIR, and ^{1}H NMR methods (Figure S2), as well as by electrospray ionization (ESI) mass spectrometry (Figure S3) and elemental analyses.

Well-defined and sharp peaks in the ^{1}H NMR spectra in CD_3CN confirm the diamagnetic nature ($3d^6$ $^{LS}Co^{III}$) of these complexes. Figure 1 shows the ORTEP representations of crystals for **2**, **3**, and **4**, and relevant bond lengths and crystallographic parameters are summarized in Tables T1 and T2 (Supporting Information, SI). These complexes are pseudo-octahedral in which two N_{amine}, one N_{py}, and one Cl define the basal plane and two N_{py} atoms occupy the axial

[*] D. Basu, Dr. S. Mazumder, X. Shi, H. Baydoun, Prof. H. B. Schlegel, Prof. C. N. Verani
Department of Chemistry, Wayne State University
5101 Cass Ave, Detroit, MI 48202 (USA)
E-mail: cnverani@chem.wayne.edu
Homepage: http://chem.wayne.edu/veranigroup/
Dr. J. Niklas, Dr. O. Poluektov
Argonne National Laboratory, Chemistry Division, E117
9700 South Cass Ave. Argonne, IL 60439 (USA)

[**] This material is based upon work supported by the U.S. Department of Energy, Office of Science, Office of Basic Energy Sciences under award number DE-SC0001907 to C.N.V. and H.B.S., including financial support for D.B. (synthesis and catalysis), H.B. (crystallography), S.M. and X.S. (calculations). Prof. John F. Endicott is acknowledged for critical discussions.

Supporting information for this article is available on the WWW under http://dx.doi.org/10.1002/anie.201409813.

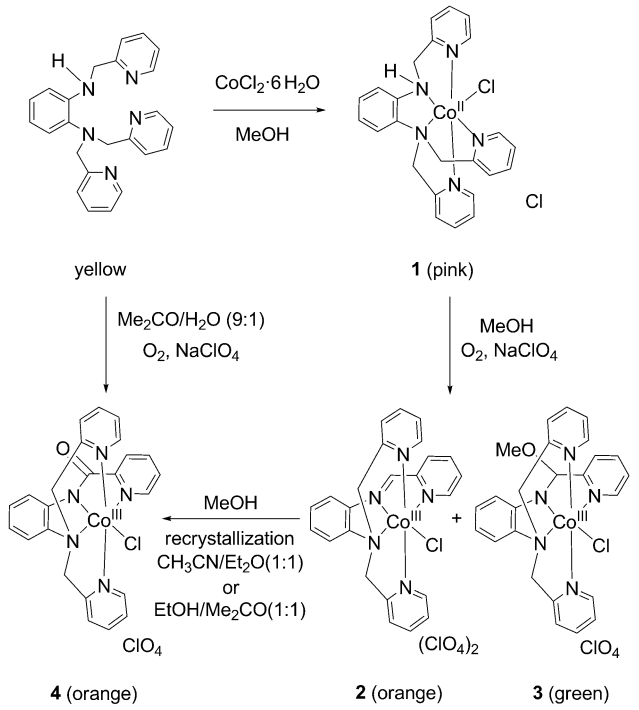

Scheme 1. Synthesis of Co^{III} complexes **2**, **3**, and **4**.

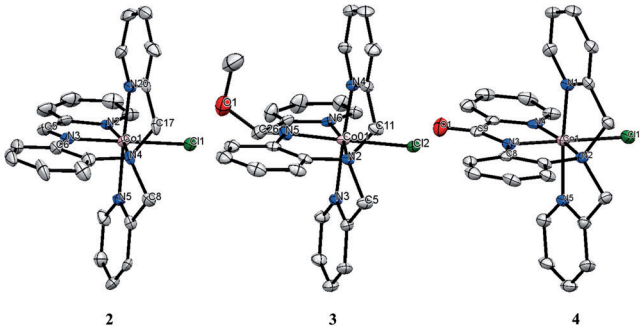

Figure 1. ORTEP representations of **2**–**4** at 50% probability.

positions. The amine moiety of the ligand framework is oxidized to imine in **2**, as observed by a shorter 1.28 Å C(5)–N(3) bond than a regular C–N bond length (~1.5 Å). Species **3** is obtained through addition of a methoxide to C(26) from the solvent methanol. The C(26)–N(5) bond length increases from 1.28 Å in **2** to 1.42 Å and N(5) becomes formally negative. Both the imine and methoxy functionalities in **2** and **3** are converted into an amide moiety in **4.** The N(3) amide atom is also negatively charged and coordinated to Co^{III} at 1.88 Å; this bond is the strongest among all the Co–N bonds of the species. The C(9)=O(1) moiety is 1.23 Å long and the C(9)–N(3) distance of 1.35 Å is shorter than a regular C–N bond, suggestive of significant π-conjugation in the ligand framework. Isolation of the methoxy species **3** demonstrates the susceptibility of the imine function in **2** to undergo facile nucleophilic attack from the solvent. Similarly, to explain the amide conversion from **2** to **4**, a hydroxy intermediate must be invoked by addition of adventitious water present in the solvent to the imine moiety of **2**. This step has been

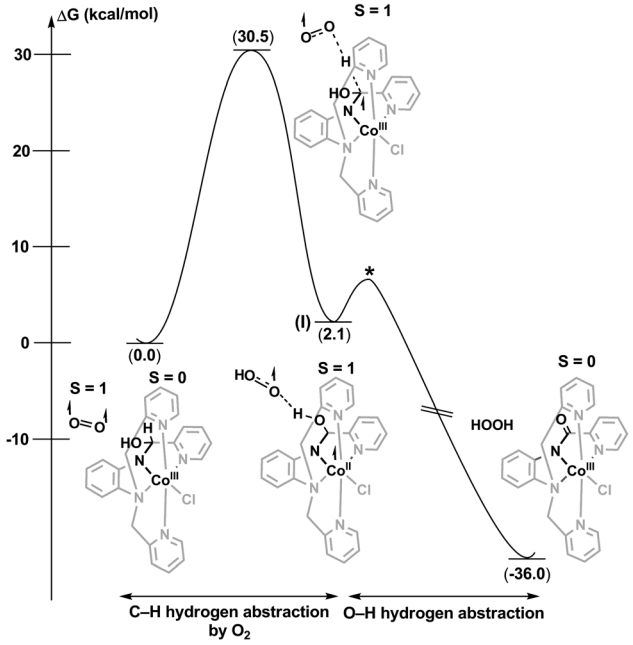

Figure 2. Reaction energy profile for the hydroxy to amide conversion in MeCN. The transition state * is not explicitly located.

documented.[9] A detailed density functional theory (DFT)[10] study was also performed to evaluate details of the hydroxy to amide conversion mechanism (Figure 2). Calculations indicate that the transformation requires atmospheric $^3O_2$ to react with the C–H function of the intermediate hydroxy complex. The C–H hydrogen abstraction event is rate-limiting and nearly isoenergetic as the resulting intermediate **I** is about 2 kcal mol^{-1} higher than the starting hydroxy complex. In species **I** the hydroperoxo radical (·OOH) is weakly bonded to the hydroxy and the unpaired electron generated on the ligand is transferred to the metal center reducing it to Co^{II}. Thus, the metal center helps stabilize the radical intermediate **I** and makes the C–H hydrogen removal event nearly isoenergetic.[9] An intersystem crossing (triplet to singlet surface) from species **I** followed by the removal of the hydroxy hydrogen by the hydroperoxo radical gives rise to the amide complex **4** and the overall process is favored by about 38 kcal mol^{-1}. Geometry optimization of intermediate **I** on the singlet surface results in the transfer of the hydroxy hydrogen from the metal complex to the hydroperoxo radical, giving rise to **4**.

Other mechanistic pathways probed for the formation of **4** can be found in Figure S4 a–c. Experimental results showed that the conversion of **2** and **3** to the amide **4** does not take place in the absence of oxygen (Figure S5). Inspection of the optimized geometry of **3** shows that a direct S_N2 attack on the carbon atom bearing the methoxy function by a water molecule is also not feasible because of steric crowding imposed by one of the pyridine rings (Figure S6). As a result, conversion of **3** to **4** must proceed through the regeneration of **2** that then undergoes water addition followed by oxidation with O_2 (Figure S6).

To prevent the initial oxidation of L^{1H} into its imine counterpart, an *N*-methylamine derivative ligand L^2 was

designed. Synthesis of the ligand was performed by the reaction of *N*-methyl phenylenediamine with picolyl chloride in the presence of NaOH and hexadecyl trimethyl ammonium chloride (Figure S7). This new ligand allowed for the complexation of a $3d^7$ Co^{II} from $CoCl_2{\cdot}6H_2O$ in methanol under aerobic conditions without the previously observed oxidation to imine. The pinkish colored $[Co^{II}(L^2)Cl]ClO_4$ (**5**) was isolated by counterion exchange with $NaClO_4$ after 2 h (Figure 3). The X-ray structure of **5** shows the Co–Cl bond

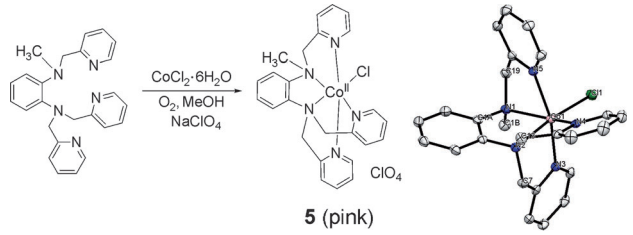

Figure 3. Synthesis of Co^{II} complex **5** and its ORTEP representation at 50% ellipsoid probability.

at 2.33 Å, thus longer than those found in **2**–**4** (Tables T1, T2, T3, and T4, SI). The complex was characterized by FTIR, ESI-MS (Figure S8), and elemental analysis. DFT calculations predict that the high-spin ($S = 3/2$) configuration is more stable than the low-spin ($S = 1/2$) configuration by 13.7 kcal mol^{-1}. Indeed, the ^1H NMR spectrum yielded broad and shifted peaks indicating a paramagnetic nature of the complex.

The electron paramagnetic resonance (EPR) spectrum of **5** in MeCN was taken at 4 K and confirms the species as $^{HS}Co^{II}$ in a pseudo-octahedral environment (Figure 4a). The observed peaks are interpreted as transitions between $\Delta m_s = \pm 1/2$ sublevels and can be simulated with the parameters $g_1 = 6.34$, $g_2 = 3.47$, $g_3 = 1.96$, and $A_1 = 474$, $A_2 = 130$, and $A_3 = 170$ MHz. As a rule, the EPR lines for $\Delta m_s = \pm 3/2$ are not observed in noncrystalline $3d^7$ systems due to their strong orientation dependence. Comparison of the crystal structure with the calculated high-spin (Figure 4b) and low-spin (Figure 4c) configurations also find a much better agreement with the HS species, showing deviations in the metal–ligand bond lengths between 0.03–0.08 Å, whereas the same deviation for an LS species varies from 0.03–0.34 Å (Figure S9).

Inspection of the geometries of the Co^{III} **2** and the Co^{II} **5** complexes shows a change in the conformation of the ligand framework. This reversal of the conformational stability is imposed by the change of the ligand from imine to *N*-methylamine, rather than by the change of the oxidation state from Co^{III} to Co^{II} (Figures S10 and S11). The UV/Vis spectra of the Co^{III} complexes **2**–**4** in MeCN are shown in Figure S12 and Table T5 (SI). They are dominated by intense intraligand UV processes along with faint visible processes associated with d–d transitions. The imine **2** and amide **4** show absorptions at 490 nm (20400 cm^{-1}, $\varepsilon = 240\,M^{-1}cm^{-1}$) and 488 nm (20500 cm^{-1}, $\varepsilon = 320\,M^{-1}cm^{-1}$), respectively, associated with the $^1T_{2g}(I) \leftarrow {}^1A_{1g}(D)$ transition of an ideal octahedral field.[11] These species absorb in the blue region and are characterized by a faint orange color. The methoxy species **3** shows a lower energy absorption at 667 nm (15000 cm^{-1}, $\varepsilon = 410\,M^{-1}cm^{-1}$) associated with $^1T_{2g}(I) \leftarrow {}^1A_{1g}(D)$. It absorbs in the red region and is green colored. On the other hand, the pinkish color observed for the $^{HS}Co^{II}$ species **5** is the result of an absorption in the green region at 504 nm (19800 cm^{-1}, $\varepsilon = 46\,M^{-1}cm^{-1}$) associated with an idealized $^4T_{1g}(P) \leftarrow {}^4T_{1g}(F)$ process.[11b]

The cyclic voltammetry (CV) profile for **2** in dry MeCN shows two reversible and two quasi-reversible processes at −0.27, −1.16, −2.01, and −2.12 $V_{Fc/Fc+}$ (Figure 5). Complex **4** shows two reversible and one irreversible process at −0.69, −1.99, and −2.41 $V_{Fc/Fc+}$, whereas two reversible and one quasi-reversible process were found at −0.02, −1.92, and −2.39 $V_{Fc/Fc+}$ for species **5** (Figure 5). CV profiles of **1** and **3** are shown in Figure S13.

The reduced species generated at affordable potentials for the chemically robust species **4** and **5** are of immense interest to proton and water reduction, and a detailed electronic

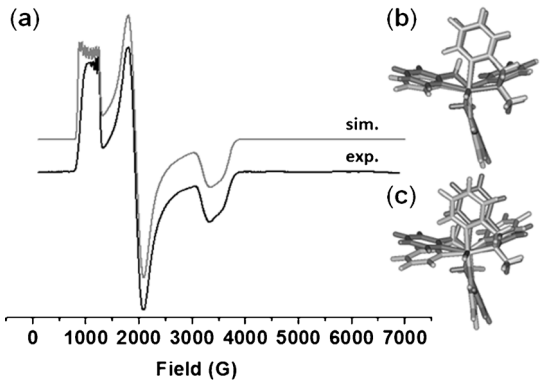

Figure 4. a) EPR spectrum of ^{HS}**5** ($S = 3/2$) in MeCN. Comparison of the crystal structure with the calculated HS (b) and LS (c) species.

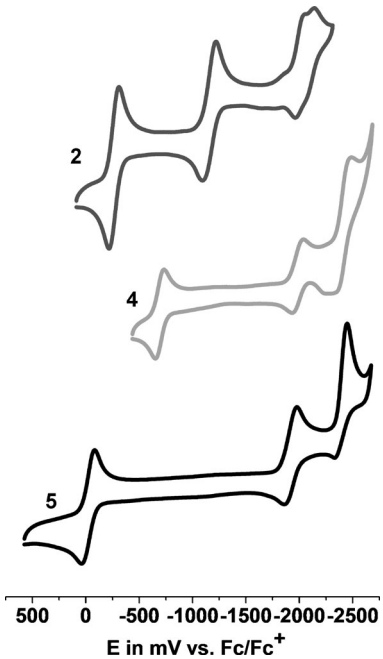

Figure 5. Cyclic voltammetry profiles of **2**, **4**, and **5** in dry MeCN.

characterization is offered here. Important CV parameters for the reduced analogues of **2**–**5** are presented in Table T6 (SI) and electronic and energetic analyses are shown in Figure S14. Mulliken spin density analysis finds the first reduction event associated to the Co^{III}/Co^{II} couple for **4** yielding a $3d^7$ $^{HS}Co^{II}$ center. Occupation of the antibonding metal-based and idealized e_g* molecular orbitals (MOs) increases the metal–ligand bond length in the Co^{II} species and leads to a rapid loss of the chloro ligand in the newly formed six-coordinate Co^{II} complex. This loss is energetically favorable by 5.5 kcal mol^{-1} and results in a 3d five-coordinate $^{HS}Co^{II}$ species. Because of the presence of a planar and conjugated amide framework, some degree of redox non-innocence behavior is shown by the ligand during the second reduction event (Figure S14). Complex **5** undergoes oxidation at −0.02 V (Co^{II} to Co^{III}), whereas the first reduction event happens at −1.92 V. Calculations suggest that this reduction event is metal-based and results in a $3d^8$ Co^{I} center. Loss of the chloro ligand from Co^{I} complex is favored by 5.4 kcal mol^{-1}. On the other hand, chloride elimination from the six-coordinate Co^{II} analogue is unfavorable by 4.9 kcal mol^{-1}.

The electrocatalytic behavior was investigated with complexes **4** and **5** due to their stability and robust nature. The weak organic acids, acetic acid (HOAc; Figure 6a) and triethyl ammonium chloride (Et_3NHCl; Figure S15) were used as proton sources. A catalytic peak was found near the second reduction process for **4** upon addition of various equivalents of HOAc in MeCN (Figure 6a). An observed catalytic current of 200 μA was measured after addition of 10 equiv of HOAc and the overpotential was 0.740 V when the homoconjugation effect of the acid was considered.[12] The rate of H_2 generation (k_{obs}) was 7.39 s^{-1} and the identity of dihydrogen was confirmed by bulk electrolysis at −1.7 $V_{Ag/AgCl}$. A turnover number (TON) of 15.44 after 3 h was calculated with 100 equiv of acid. Faradaic efficiency was measured to be approximately 90%. Control experiments with HOAc in MeCN in absence of **4** exhibited catalytic peaks at significantly more negative potentials (Figure S16), thus validating the role of that species as a catalyst. Comparison of the charge (Q) versus time (t) plots in the presence and absence of **4** confirms the catalytic activity of the complex (inset: Figure 6a). Electrocatalytic measurements with complex **5** found a catalytic peak close to the second redox couple (Figure 6b) as observed with **4**. The catalytic current and k_{obs} are 150 μA and 4.29 s^{-1}, respectively, in the presence of 10 equiv of HOAc. An overpotential of 0.69 V was found and H_2 evolution was confirmed by electrolysis at −1.7 $V_{Ag/AgCl}$. A TON of 14.35 was observed after 3 h with 100 equiv of acid and Faradaic efficiency was 75%. Control experiments (Figure S16) and Q versus t plots (inset: Figure 6b) confirm the catalytic behavior of **5**. Comparison of the electrocatalytic behavior of **4** and **5** with that of a blank solution is shown in Figure S17.

The ultimate goal of electrocatalytic H_2 generation from neutral water (pH 7) in phosphate buffer (1M) was attained with **4** and **5** (Figure 7a and 7b). The catalytic peak appears at an onset overpotential of 0.55 V for **4**. Electrolysis at −1.7 $V_{Ag/AgCl}$ yielded a TON of 1,615 over 3 h with Faradaic efficiency of 95%. The TON reaches over 7000 after 18 h

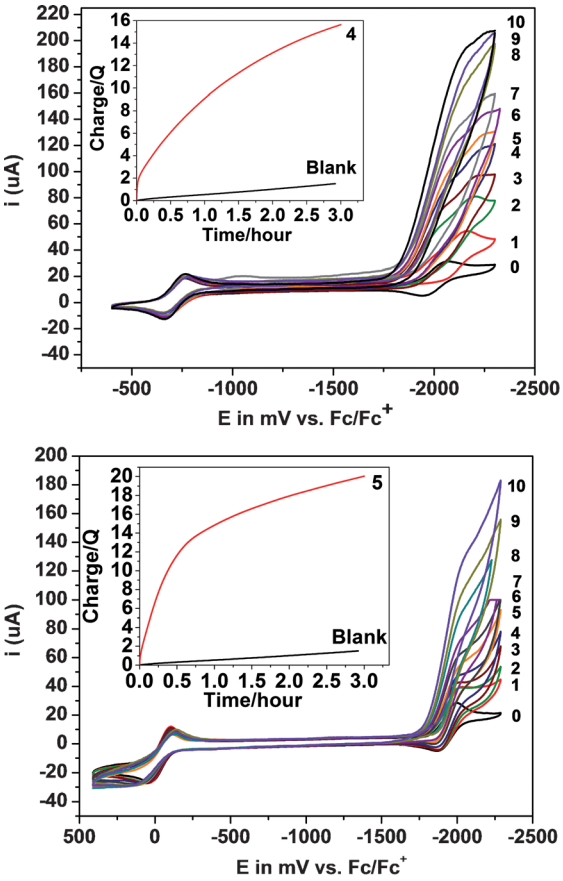

Figure 6. CV experiments of H_2 generation by **4** (a) and **5** (b) in MeCN. The numbers 0–10 indicate the HOAc equiv used in comparison to the complex. Insets: Charge versus time plots during the bulk electrolysis of **4** and **5** (applied potential: −1.7 $V_{Ag/AgCl}$). Complex: 4 μmol; HOAc: 0.4 mmol during electrolysis.

without obvious signs of catalyst decomposition, as suggested by the straight Q vs. t plots shown as insets in Figure 7 and in Figure S18. The catalytic peak for **5** appears at the slightly more positive onset overpotential of 0.70 V, and electrolysis at −1.7 $V_{Ag/AgCl}$ confirmed dihydrogen generation. The TON and Faradaic efficiency were calculated to be 1400 and 95%, respectively, over 3 h. No obvious decomposition of the catalyst **5** was observed after 18 h, when the TON reaches over 6000 and a linear Q versus t plot persisted (Figure S19). Control experiments generate some dihydrogen at more negative potentials than those with **4** and **5**. Charge consumption over time is much higher with both the complexes than that with the blank solution. Comparison of the electrocatalytic behavior of **4** and **5** in water is shown in Figure S20. Relevant catalytic parameters are reported in Table T7 (SI). Another control experiment was performed to further probe the catalytic nature of species **4** and **5**; the catalytic activity of those species was compared with that of a cathodically polarized working glassy carbon electrode after catalysis, rinsed and dipped in fresh electrolyte. The results, shown in Figures S21 and S22, confirm the need for the catalysts to decrease the overpotential for H_2 formation. The robustness of the catalysts was also investigated by spectroscopic and spectrometric means (Figures S23 and S24). Both species

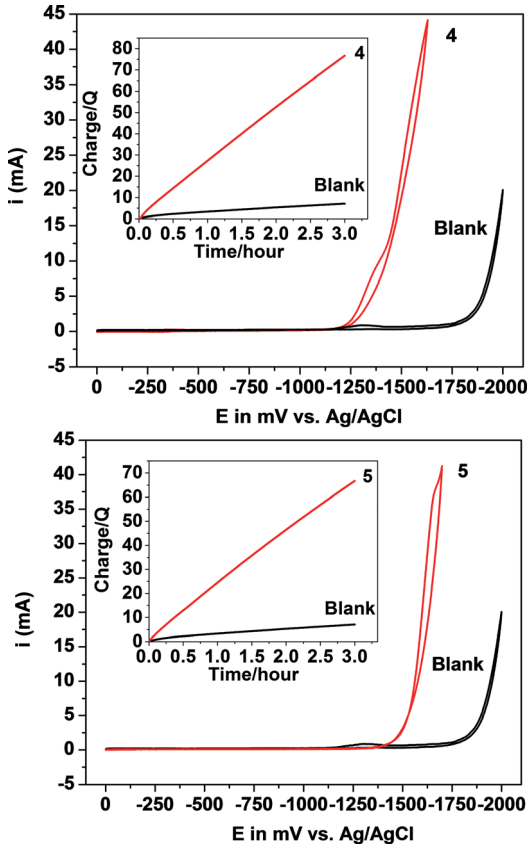

Figure 7. CV experiments of H_2 generation by **4** (a) and **5** (b) from water (pH 7 with 1 M phosphate buffer). Insets: charge versus time plots during the bulk electrolysis of **4** and **5** (applied potential: $-1.7\ V_{Ag/AgCl}$). Complex: 0.2 μmol during electrolysis.

show similar aerobic UV/Vis spectra before and after bulk electrolysis, and the presence of ESI(+)-MS peaks with $m/z =$ 488 and 489 associated with the cations $[4]^+$ and $[5]^+$, respectively. Interestingly, species **4** displays a blue-shifted spectrum after anaerobic bulk electrolysis that is converted to the original spectrum in the presence of air. This observation suggests that the Co^{III} species **4** is a procatalyst in good agreement with the calculated catalytic cycles discussed in Figures 8 and S25.

Mechanisms of electrocatalytic H_2 evolution by **4** and **5** have been evaluated by DFT calculations. Figure 8 describes the catalytic pathway for complex **4** in MeCN. The five-coordinate Co^{II} species, generated after dissociation of the chloro ligand, undergoes reduction to the corresponding Co^{I} complex. The reduction potential is calculated as $-1.83\ V_{Fc/Fc+}$. Uptake of a proton by the Co^{I} complex is favorable by 22.5 kcal mol^{-1} and results in the six-coordinate Co^{III}–H^- complex, which gets reduced to the more reactive $^{HS}Co^{II}$–H^- species. The latter is high-spin in nature and occupation of the idealized e_g* MOs weakens the metal–ligand interactions. The Co–H bond elongates from 1.49 Å in the $^{LS}Co^{III}$ complex to 1.73 Å in the $^{HS}Co^{II}$ species. As a result, the hydride in the Co^{II}–H^- moiety is susceptible to heterolytic attack by an external proton. Uptake of a proton and generation of H_2 by this complex is favored by 54.0 kcal mol^{-1}

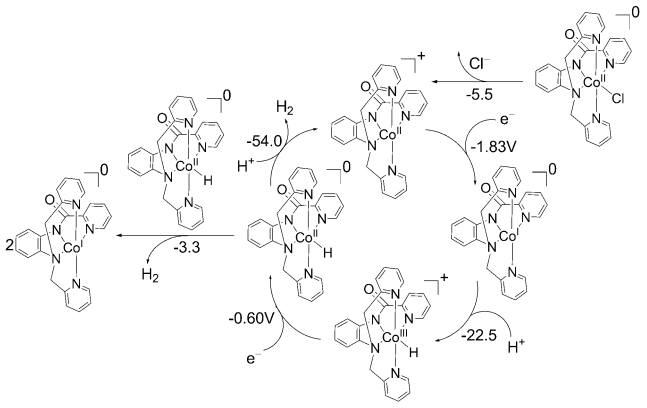

Figure 8. Catalytic mechanism of H_2 generation by **4** in MeCN. It involves a Co^{II}–H^- species that undergoes protonation to generate H_2. The calculated energetics for all events is reported as free energy changes in kcal mol^{-1}.

(Figure 8), regenerating the five-coordinate Co^{II} complex to restart the catalytic cycle. The reaction of a proton with Co^{II}–H is expected to be activationless.[5c] The homolytic pathway by the combination of two Co^{II}–H complexes is significantly less exothermic compared to the heterolytic mechanism. A proton-coupled electron transfer (PCET) event is not invoked for the Co^{II}/Co^{III}–H^- transformation, because no anodic shift was found in the experimental electrocatalytic measurement of **4** upon decrease of pH. Complex **5** follows a similar catalytic mechanism as described in Figure S25; however, the involvement of a Co^{I}/Co^{II}–H PCET mechanism may be relevant. The generation of H_2 in both mechanisms favors a heterolytic pathway with another proton, rather than a bimolecular mechanism through the combination of two Co^{II}–H^- complexes.

In conclusion, we have described the syntheses and characterization of a series of pentadentate, pyridine-rich Co complexes **2**–**5** with imine, methoxy, amide, and *N*-methylamine functionalities. The methoxy and amide species arise from the imine complex **2** through reaction with methanol and water solvent, respectively. The Co^{III} imine **2** arises from aerial oxidation of the corresponding Co^{II} amine species **1**. Introduction of an *N*-methyl function in **1** inhibits this oxidation and yields the $^{HS}Co^{II}$ *N*-methylamine **5**. Electrocatalytic experiments with **4** and **5** generate H_2 with TONs of 15.44 and 14.35, respectively, after 3 h in the presence of acetic acid in MeCN solutions. Remarkably, **4** and **5** are excellent water reduction catalysts with TONs of 7000 and 6000, respectively, after 18 h. The present TONs insert these two species among a select group of top catalysts for water reduction. Catalytic mechanisms obtained by DFT calculations involve the formation of a Co^{III}–H^- species that undergoes further reduction followed by protonation of the hydride on the cobalt center. Current efforts in our groups aim to enable the use of these species for photocatalysis.

Received: October 6, 2014
Revised: November 25, 2014
Published online: ■■ ■■, ■■■■

Keywords: cobalt complexes · Co^{I}–H^{-} species · proton reduction · pyridine ligands · water reduction

[1] a) J. A. Turner, *Science* **2004**, *305*, 972 – 974; b) N. S. Lewis, D. G. Nocera, *Proc. Natl. Acad. Sci. USA* **2006**, *103*, 15729 – 15735.
[2] a) A. D. Wilson, R. H. Newell, J. T. McNevin, J. T. Muckerman, M. R. Dubois, D. L. Dubois, *J. Am. Chem. Soc.* **2006**, *128*, 358 – 366; b) P. A. Jacques, V. Artero, J. Pecaut, M. Fontecave, *Proc. Natl. Acad. Sci. USA* **2009**, *106*, 20627 – 20632; c) L. Chen, M. Wang, F. Gloaguen, D. Zheng, P. Zhang, L. Sun, *Inorg. Chem.* **2013**, *52*, 1798 – 1806.
[3] P. Connolly, J. H. Espenson, *Inorg. Chem.* **1986**, *25*, 2684 – 2688.
[4] a) H. Xile, B. M. Cossairt, B. S. Brunschwig, N. S. Lewis, J. C. Peters, *Chem. Commun.* **2005**, 4723 – 4725; b) M. Razavet, V. Artero, M. Fontecave, *Inorg. Chem.* **2005**, *44*, 4786 – 4795; c) H. Xile, B. S. Brunschwig, J. C. Peters, *J. Am. Chem. Soc.* **2007**, *129*, 8988 – 8998; d) C. Baffert, V. Artero, M. Fontecave, *Inorg. Chem.* **2007**, *46*, 1817 – 1824; e) A. Bhattacharjee, E. S. Andreiadis, M. C. Kerlidou, M. Fontecave, M. J. Field, V. Artero, *Chem. Eur. J.* **2013**, *19*, 15166 – 15174.
[5] a) B. H. Solis, S. Hammes-Schiffer, *J. Am. Chem. Soc.* **2011**, *133*, 19036 – 19039; b) B. H. Solis, S. Hammes-Schiffer, *Inorg. Chem.* **2011**, *50*, 11252 – 11262; c) J. T. Muckermann, E. Fujita, *Chem. Commun.* **2011**, *47*, 12456 – 12458; d) B. Solis, Y. Yu, S. Hammes-Schiffer, *Inorg. Chem.* **2013**, *52*, 6994 – 6999.
[6] a) J. P. Bigi, T. E. Hanna, W. H. Harman, A. Chang, C. J. Chang, *Chem. Commun.* **2010**, *46*, 958 – 960; b) B. D. Stubbert, J. C. Peters, H. B. Gray, *J. Am. Chem. Soc.* **2011**, *133*, 18070 – 18073; c) Y. Sun, J. P. Bigi, N. A. Piro, M. L. Tang, J. R. Long, C. J. Chang, *J. Am. Chem. Soc.* **2011**, *133*, 9212 – 9215; d) C. F. Leung, Y. Z. Chen, H. Q. Yu, S. M. Yiu, C. C. Ko, T. C. Lau, *Int. J. Hydrogen Energy* **2011**, *36*, 11640 – 11645; e) W. M. Singh, T. Baine, S. Kudo, S. Tian, X. A. N. Ma, H. Zhou, N. J. DeYonker, T. C. Pham, J. C. Bollinger, D. L. Baker, B. Yan, C. E. Webster, X. Zhao, *Angew. Chem. Int. Ed.* **2012**, *51*, 5941 – 5944; *Angew. Chem.* **2012**, *124*, 6043 – 6046; f) A. E. King, Y. Surendranath, N. A. Piro, J. P. Bigi, J. R. Long, C. J. Chang, *Chem. Sci.* **2013**, *4*, 1578 – 1587; g) M. Nippe, R. S. Khnayzer, J. A. Panetier, D. Z. Zee, B. S. Olaiya, M. Head-Gordon, C. J. Chang, F. N. Castellano, J. R. Long, *Chem. Sci.* **2013**, *4*, 3934 – 3945; h) P. Zhang, M. Wang, F. Gloaguen, L. Chen, F. Quentel, L. Sun, *Chem. Commun.* **2013**, *49*, 9455 – 9457; i) W. M. Singh, M. Mirmohades, R. T. Jane, T. A. White, L. Hammarström, A. Thapper, R. Lomoth, S. Ott, *Chem. Commun.* **2013**, *49*, 8638 – 8640; j) L. Tong, R. Zong, R. P. Thummel, *J. Am. Chem. Soc.* **2014**, *136*, 4881 – 4884; k) K. Kawano, K. Yamauchi, K. Sakai, *Chem. Commun.* **2014**, *50*, 9872 – 9875; l) A. Call, Z. Codolà, F. Acuña-Parés, J. Lloret-Fillol, *Chem. Eur. J.* **2014**, *20*, 6171 – 6183.
[7] a) M. Lanznaster, H. P. Hratchian, M. J. Heeg, L. M. Hryhorczuk, B. R. McGarvey, H. B. Schlegel, C. N. Verani, *Inorg. Chem.* **2006**, *45*, 955 – 957; b) M. Lanznaster, M. J. Heeg, G. T. Yee, B. R. McGarvey, C. N. Verani, *Inorg. Chem.* **2007**, *46*, 72 – 78; c) M. M. Allard, J. A. Sonk, M. J. Heeg, B. R. McGarvey, H. B. Schlegel, C. N. Verani, *Angew. Chem. Int. Ed.* **2012**, *51*, 3178 – 3182; *Angew. Chem.* **2012**, *124*, 3232 – 3236; d) M. M. Allard, F. R. Xavier, M. J. Heeg, H. B. Schlegel, C. N. Verani, *Eur. J. Inorg. Chem.* **2012**, 4622 – 4631; e) L. D. Wickramasinghe, M. M. Perera, L. Li, G. Mao, Z. Zhou, C. N. Verani, *Angew. Chem. Int. Ed.* **2013**, *52*, 13346 – 13350; *Angew. Chem.* **2013**, *125*, 13588 – 13592; f) L. D. Wickramasinghe, S. Mazumder, S. Gonawala, M. M. Perera, H. Baydoun, B. Thapa, L. Li, L. Xie, G. Mao, Z. Zhou, H. B. Schlegel, C. N. Verani, *Angew. Chem. Int. Ed*. **2014**, DOI: 10.1002/anie.201408649; *Angew. Chem.* **2014**, DOI: 10.1002/ange.201408649; g) D. Basu, M. M. Allard, F. R. Xavier, M. J. Heeg, R. Staples, H. B. Schlegel, C. N. Verani, submitted to *Inorg. Chem*.
[8] M. Sato, Y. Mori, T. Iida, *Synthesis* **1992**, 539 – 540.
[9] L. A. Tyler, M. M. Olmstead, P. K. Mascharak, *Inorg. Chem.* **2001**, *40*, 5408 – 5414.
[10] R. G. Parr, W. Yang, *Density-functional theory of atoms and molecules*, Oxford University Press, New York, **1989**.
[11] a) C. J. Ballhausen, *Introduction to Ligand Field Theory*, McGraw Hill, New York, **1962**, pp. 259 – 260; b) B. N. Figgis, M. A. Hitchman, *Ligand Field Theory and its Applications*, Wiley-VCH, New York, **2000**, pp. 139 – 140; B. N. Figgis, M. A. Hitchman, *Ligand Field Theory and its Applications*, Wiley-VCH, New York, **2000**, pp. 209 – 210.
[12] V. Fourmond, P. A. Jacques, M. Fontecave, V. Artero, *Inorg. Chem.* **2010**, *49*, 10338 – 10347.

Communications

Water Reduction

D. Basu, S. Mazumder, X. Shi, H. Baydoun, J. Niklas, O. Poluektov, H. B. Schlegel,* C. N. Verani* _____ ■■■■–■■■■

Ligand Transformations and Efficient Proton/Water Reduction with Cobalt Catalysts Based on Pentadentate Pyridine-Rich Environments

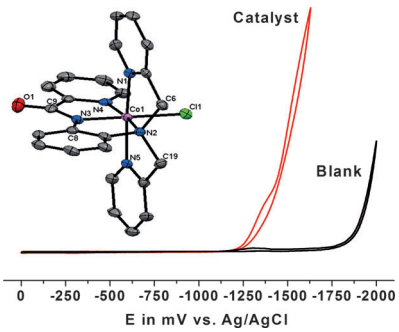

Pyridine and cobalt: A series of cobalt complexes with pentadentate pyridine-rich ligands is studied both for their ligand transformations as well as for their catalytic activity toward proton and water reduction. Turnover numbers of up to 7000 after 18 h were observed.